Multimode mediated qubit-qubit coupling and dark-state symmetries in circuit quantum electrodynamics

S. Filipp,* M. Göppl, J. M. Fink, M. Baur, R. Bianchetti, L. Steffen, and A. Wallraff
Department of Physics, ETH Zurich, CH-8093 Zurich, Switzerland
(Received 16 November 2010; published 22 June 2011)

Microwave cavities with high quality factors enable coherent coupling of distant quantum systems. Virtual photons lead to a transverse interaction between qubits when they are nonresonant with the cavity but resonant with each other. We experimentally investigate the inverse scaling of the interqubit coupling with the detuning from a cavity mode and its proportionality to the qubit-cavity interaction strength. We demonstrate that the enhanced coupling at higher frequencies is mediated by multiple higher-harmonic cavity modes. Moreover, we observe dark states of the coupled qubit-qubit system and analyze their relation to the symmetry of the applied driving field at different frequencies.

DOI: 10.1103/PhysRevA.83.063827 PACS number(s): 42.50.Ct, 03.67.Lx, 42.50.Pq, 85.35.Gv

I. INTRODUCTION

Experiments on single photons coupled strongly to single (artificial) atoms [1] allow for in-depth studies of photon-atom interactions on a single-particle level. This has been demonstrated with atoms coupled to microwave [2,3] and optical cavity fields [4,5]. In solids, strong coupling has been achieved with both quantum dots [6,7] and superconducting circuits [8]. The coherent exchange of energy between photons and atoms can be described in this diverse set of different physical systems by a generic model named after Jaynes and Cummings [9].

In circuit quantum electrodynamics (QED) experiments [8,10], superconducting quantum circuits are coupled to single microwave photons in a planar transmission line cavity. In this configuration, coupling strengths exceed decay rates by two orders of magnitude, and strong resonant coupling between a microwave cavity and a single [8,10–13] or multiple [14,15] superconducting qubits has been observed. In the case of finite detuning between a single qubit and a resonator mode, energy exchange between the individual systems is strongly suppressed due to energy conservation. In this dispersive regime, a residual interaction mediated by virtual photons induces a finite Lamb [16] and ac Stark shift [17] of the energy levels. For two qubits coupled to a common cavity field, the same mechanism leads to an interaction between the qubits [18,19] as experimentally demonstrated in [20]. This coupling has a similar form as the J coupling of interacting nuclear spins in nuclear magnetic resonance experiments (e.g., [21,22]). In contrast to local interactions, such as the direct coupling of superconducting quantum circuits [23–29], the coupling mediated via virtual resonator photons allows for a long-range interaction between two or more distant superconducting qubits. In the context of quantum information processing in the circuit QED architecture [30,31], it can be used to realize two-qubit gates [18].

In this paper we measure the qubit-qubit coupling as a function of detuning of two qubits considering a single or multiple resonator modes and characterize the symmetry properties of the coupled system. In Sec. II the interqubit coupling mechanism and its spectroscopic measurement is outlined. In Sec. III the coupling near a single resonator mode is analyzed. In Sec. IV higher-harmonic modes of the transmission line resonator are included in the analysis. The formation of a dark state at the avoided level crossing and its relation to the drive symmetry is discussed in Sec. V. Two-photon transitions from the ground to the doubly excited state observed only at qubit resonance are analyzed in Sec. VI.

II. DISPERSIVE QUBIT-QUBIT COUPLING MECHANISM

In our experiments two superconducting qubits are dispersively coupled to a microwave cavity; see Fig. 1. The quantum circuits are realized as weakly anharmonic transmon qubits [32] and the cavity is formed by a coplanar-waveguide resonator supporting several harmonic modes [33]. In the dispersive regime, the detuning $\Delta_j^{(i)} \equiv \omega_{ge}^{(i)} - \omega_j$ of both qubits with transition frequency $\omega_{ge}^{(i)}$ $(i = 1,2)$ to each resonator mode j of frequency ω_j is larger than the coupling strength $g_j^{(i)}$. The relevant Hamiltonian

$$H_J = \hbar \sum_j \left(\omega_j + \chi_j^{(1)}\sigma_z^{(1)} + \chi_j^{(2)}\sigma_z^{(2)}\right)a_j^\dagger a_j + \hbar \sum_{i=1,2} \frac{\omega_{ge}^{(i)} + \chi_j^{(i)}}{2}\sigma_z^{(i)} + \hbar J(\sigma_+^{(1)}\sigma_-^{(2)} + \sigma_+^{(2)}\sigma_-^{(1)}) \tag{1}$$

is obtained by adiabatically eliminating the direct qubit-resonator interaction of the qubits for each harmonic mode a_j in the Jaynes-Cummings Hamiltonian [18]. The first term in Eq. (1) describes the resonator modes a_j at integer multiples of the fundamental frequency, $\omega_j = (j+1)\omega_0$, shifted by the cavity pulls $\chi_j^{(i)} = (g_j^{(i)})^2/\Delta_j$ [18,35]. The second term denotes the qubit Hamiltonian comprising the Lamb shift $\chi_j^{(i)}$ of the qubit transition frequency due to the presence of virtual photons [16]. An effective qubit-qubit coupling, a flip-flop interaction, is also mediated by virtual photon exchange. This mechanism is called J coupling, or transverse exchange coupling, and is described by the third term of the Hamiltonian

*filipp@phys.ethz.ch

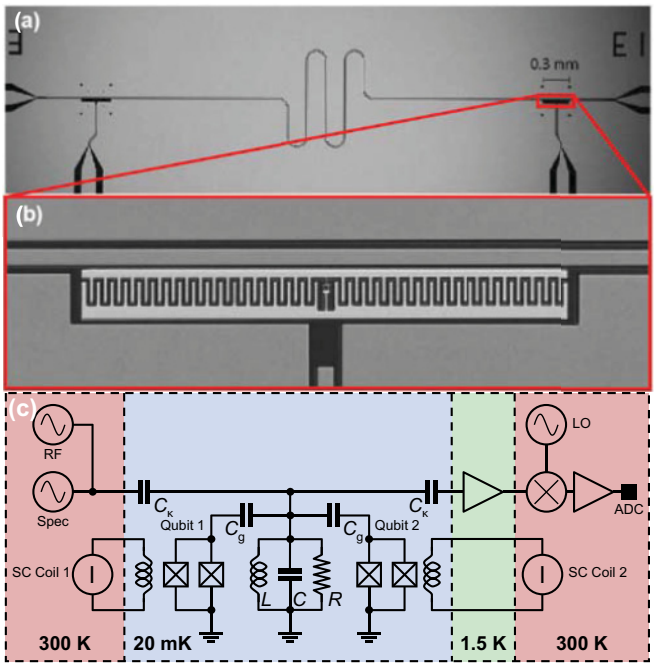

FIG. 1. (Color online) (a) Coplanar waveguide resonator coupled via finger capacitors C_κ to input and output transmission lines. Two transmons are capacitively coupled to the resonator at its ends (C_g). Additional ac-signal lines are capacitively coupled to the qubits (not used in the experiments). (b) Optical micrograph of a transmon qubit. (c) Schematic of the measurement setup. The state of the qubit is determined by measuring the transmission of the RF signal through the transmission line cavity modeled as an LCR oscillator. When a spectroscopy signal (Spec) is resonant with a qubit transition, the resonance frequency of the cavity is shifted and the change in transmission amplitude is recorded at the analog-digital converter (ADC) after down-conversion with a local oscillator (LO) [34]. The qubit frequencies can be tuned independently with superconducting coils (SC Coil 1 or 2).

with

$$J = \frac{1}{2}\sum_j g_j^{(1)} g_j^{(2)} \left(\frac{1}{\Delta_j^{(1)}} + \frac{1}{\Delta_j^{(2)}} \right). \tag{2}$$

In a different context this interaction has been used to entangle two Rydberg atoms crossing a nonresonant cavity [36,37].

The J coupling in Eq. (2) leads to an avoided level crossing of the excited qubit states [20]. At resonance between the qubits, where $\delta_q \equiv \omega_{ge}^{(1)} - \omega_{ge}^{(2)} = 0$, the size of the splitting is $2J = \hbar \sum_j 2 g_j^{(1)} g_j^{(2)} / \Delta_j$. The new eigenstates are the symmetric triplet states $|gg\rangle$, $|ee\rangle$, and $|\psi_s\rangle = (|ge\rangle + |eg\rangle)/\sqrt{2}$, as well as the antisymmetric singlet state $|\psi_a\rangle = (|ge\rangle - |eg\rangle)/\sqrt{2}$; see Fig. 2(a). In the maximally entangled states $|\psi_{s/a}\rangle$ a single excitation is shared between the two qubits. More generally, for $\delta_q \neq 0$ the eigenstates of the Hamiltonian in Eq. (1) can be parametrized as

$$\begin{aligned} |\psi_s\rangle &= \sin\theta_m |eg\rangle + \cos\theta_m |ge\rangle, \\ |\psi_a\rangle &= \cos\theta_m |eg\rangle - \sin\theta_m |ge\rangle, \end{aligned} \tag{3}$$

with the mixing angle θ_m determined by $\cos 2\theta_m = -\delta_q / \sqrt{4J^2 + \delta_q^2}$ and $\sin 2\theta_m = 2J / \sqrt{4J^2 + \delta_q^2}$. The separable qubit states $|eg\rangle$ and $|ge\rangle$ are asymptotically realized, $|\psi_a\rangle \to |eg\rangle$ and $|\psi_s\rangle \to |ge\rangle$, for large qubit-qubit detunings ($\delta_q \to \infty$), as indicated in Fig. 2(b).

Note that, for identical transmon qubits, all higher-energy eigenstates split simultaneously and the level crossing can be treated similarly. Diagonalizing the Jaynes-Cummings Hamiltonian including five transmon levels leads, however, to corrections of the magnitude J of 1% only. Moreover, since higher transmon levels are not populated in our experiments, they are neglected in the following.

We have performed two sets of experiments using samples with different parameters listed in Table I. In these experiments, the energy spectrum of the coupled qubits is probed by monitoring the transmission through the resonator while applying a spectroscopy tone at frequency ω_d [17]. For the spectroscopy measurement shown in Fig. 2 (b), the second qubit frequency $\omega_{ge}^{(2)}$ is kept fixed and the first qubit frequency $\omega_{ge}^{(1)}$ is swept across the avoided crossing by changing its flux bias using external coils. The value of J can be extracted from a fit of the upper and lower branch of the avoided crossing to the function

$$f\left(\omega; \omega_{ge}^{(2)}, J\right) = \left(\left(\omega + \omega_{ge}^{(2)}\right) \pm \sqrt{\left(\omega_{ge}^{(2)} - \omega\right)^2 + 4J^2} \right) / 2, \tag{4}$$

where ω is in this parameter regime an approximately linear function of the flux Φ threading the first qubit loop. The fit parameters are the transition frequency $\omega_{ge}^{(2)}$ of the second qubit and the coupling strength J. Both are determined with a precision of typically better than 0.5 MHz. In this particular example we find $\omega_{ge}^{(2)}/(2\pi) = 5.210$ GHz and $J/(2\pi) = 10.06$ MHz.

Two additional features are observed in Fig. 2(b). First, an extra spectroscopic line centered between the upper and the lower branch appears at higher drive powers. This is a signature of a two-photon transition from the ground state $|gg\rangle$ to the doubly excited state $|ee\rangle$ of the coupled qubit system that is allowed only when both qubits are in resonance. This is discussed further in Sec. VI. As a second feature, the upper branch shows a transition to a dark resonance at the avoided crossing, which can be explained by the symmetry of the states with respect to the spectroscopic drive, as discussed in Sec. V.

TABLE I. Parameters of samples A and B as determined from independent measurements. ω_0 denotes the fundamental frequency, κ the cavity decay rate, $E_C^{(1,2)}$ the charging energy, $E_J^{(1,2)}$ the maximum Josephson energy, and $g_0^{(1)}$ and $g_0^{(2)}$ the coupling strength to the fundamental cavity mode of qubits 1 and 2, respectively.

Parameter	Sample A	Sample B
$\omega_0/(2\pi)$	6.44 GHz	3.34 GHz
$\kappa/(2\pi)$	1.57 MHz	1.91 MHz
$E_C^{(1)}/h$	232 MHz	148 MHz
$E_C^{(2)}/h$	233 MHz	153 MHz
$E_J^{(1)}/h$	35 GHz	409 GHz
$E_J^{(2)}/h$	38 GHz	375 GHz
$g_0^{(1)}/(2\pi)$	133 MHz	43 MHz
$g_0^{(2)}/(2\pi)$	134 MHz	42 MHz

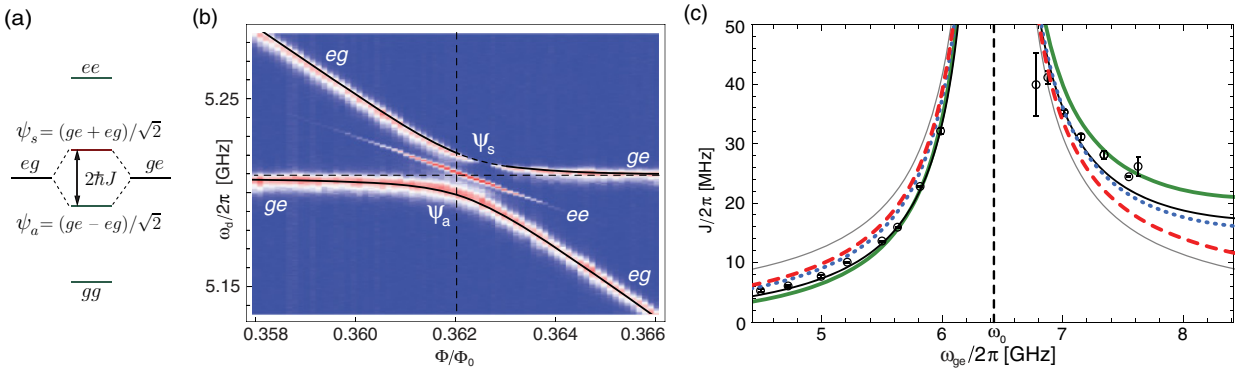

FIG. 2. (Color online) (a) Energy level diagram of two transversely coupled qubits. (b) Spectroscopic measurement of the avoided level crossing in sample A as a function of normalized flux Φ/Φ_0 threading the first qubit loop with the second qubit at a fixed frequency. The solid lines indicate energy levels calculated from a diagonalization of the two-qubit Jaynes-Cummings Hamiltonian. (c) Experimentally extracted value of the coupling strength J as a function of qubit frequency (circles). Lines indicate calculated values of $J(\omega_{ge})$ for a model including one resonator mode with frequency-independent (thin solid gray line) or frequency-dependent coupling strength (dashed red line). Theoretical predictions including four (thick solid green line) and five resonator modes (dotted blue line). The thin solid black line comprises finite-size effects of the transmons using 60 resonator modes.

III. COUPLING TO THE FUNDAMENTAL RESONATOR MODE

According to Eq. (2) the coupling $J = \hbar g^{(1)} g^{(2)}/\Delta$ scales inversely with the detuning $\Delta = \Delta^{(1)} = \Delta^{(2)}$, considering only a single resonator mode. We have spectroscopically measured the avoided crossing between the two qubits by varying the detuning Δ from the fundamental mode of the resonator of sample A. The corresponding sample parameters are listed in Table I. The measured values of J shown in Fig. 2(c) are determined for each detuning from a fit as described in Sec. II.

Considering only the relevant resonator mode closest in frequency with constant g, the strength of the interqubit coupling is expected to be symmetric about the resonator frequency [Eq. (2); thin gray line in Fig. 2(c)]. The asymmetry in the data can partly be accounted for by including the frequency dependence of the coupling g, as explained in Appendix A. It follows from the transition matrix elements that J scales approximately linearly with the transition frequency ω_{ge} of the qubits. This scaling leads to an asymmetry of the J coupling around the resonance frequency ω_0 that improves the agreement with the data [dashed red line, Fig. 2(c)]. To verify that the remaining discrepancy does not originate from the dispersive approximation, we have determined J also by numerically diagonalizing the full generalized Jaynes-Cummings Hamiltonian (not shown). This calculation agrees with the dispersive model within the errors of the experimentally observed values of J.

To achieve a better agreement, higher harmonics of the resonator have to be considered. Similarly, the consideration of higher-order transverse modes in optical cavities have led to improved understanding of cavity QED experiments with Bose-Einstein condensates (BECs) [38]. The particular implementation of our resonator as an open-ended coplanar waveguide supports higher harmonics at integer multiples of the fundamental frequency [33], see Fig. 3(a). Each of these higher modes provides a channel for the exchange of virtual photons between the qubits determined by the detuning $\Delta_j^{(i)}$ and the coupling $g_j^{(i)}$ to the harmonic mode j as indicated in Fig. 3(b). Above the fundamental mode, the coupling to the first harmonic mode $j = 1$ contributes significantly to the qubit-qubit coupling, which results in an asymmetry with respect to the detuning. Including four modes in Eq. (2) to determine the expected value of J, good agreement with data is obtained [thick green line, Fig. 2(c)].

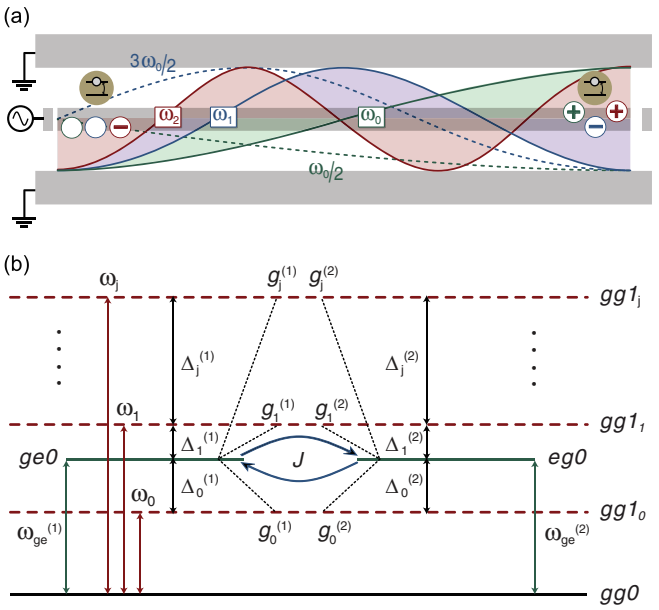

FIG. 3. (Color online) (a) Spatial mode structure of a coplanar waveguide resonator. Qubits are positioned at opposite ends of the $\lambda/2$ resonator with coupling of alternating sign, $g_j^{(1)} = (-1)^{j+1} g_j^{(2)}$ to the jth resonator mode at frequency ω_j. (b) Energy level diagram and coupling scheme for two qubits with transition frequencies $\omega_{ge}^{(1)}$ and $\omega_{ge}^{(2)}$ coupled to a transmission line cavity with fundamental frequency ω_0. Energy levels with a photon in the jth resonator mode ($gg1_j$) or a qubit excitation (ge0 or $eg0$) are shown. The interaction strength J depends on the detunings $\Delta_j^{(i)}$ and the coupling strengths $g_j^{(i)}$ of both qubits ($i = 1,2$) to the resonator mode j.

It is important to also consider the alternating sign of the electric fields at the qubits' position. As depicted schematically in Fig. 3(a), the electric field of the fundamental and higher even modes ($j = 0,2,4,\ldots$) always have opposite sign (i.e., a relative phase of π) at either end of the microwave cavity, whereas odd modes ($j = 1,3,5,\ldots$) have equal sign. Thus, higher harmonics add with different signs to the effective coupling strength.

A priori, the sum in Eq. (2) has to be extended over all modes. The sum does, however, not converge, as discussed also in the context of Purcell-limited qubit decay rates in [39]. The proportionality of the coupling $g_j^{(1)} g_j^{(2)} \propto \omega_j = (j+1)\omega_0$ Eq. (A2) together with the same proportionality of the detuning $\Delta_j \propto (j+1)\omega_0$ for large j leads to an nonconverging series alternating between the two values

$$J_{\mathrm{even}} = \hbar \sum_{j=0}^{2k} (-1)^{j+1} \frac{g_j^2}{\Delta_j} \text{ and } J_{\mathrm{odd}} = \hbar \sum_{j=0}^{2k+1} (-1)^{j+1} \frac{g_j^2}{\Delta_j}. \quad (5)$$

Apparently, a cutoff frequency has to be imposed to obtain physical results. In Fig. 2(c) we have also included a plot of J_{even} when terminating the sum at the fourth harmonic ($k = 2$, the fifth mode; dotted blue line). It is observed that the difference between an even and odd number of modes is significant—up to 25% of the coupling strength. We have verified that this is not an artifact of the dispersive model by numerically diagonalizing the Jaynes-Cummings Hamiltonian.

In summary, in this set of measurements we observe enhancement of the J coupling, inversely proportional to the detuning of the qubits to the cavity mode. The asymmetry around the mode is attributed to higher harmonic modes that contribute to the measured (renormalized) J. However, to compute the coupling strength the number of included modes has to be restricted by imposing a high-frequency cutoff. Note that these considerations also affect a precise determination of Lamb and ac Stark shifts, if the multimode structure is to be accurately considered. Physically, there are several mechanisms conceivable. First, the electric field across the transmon averages out when the wavelength of the photons becomes comparable to the size of the transmon ($\sim$300 μm) at a frequency of about 400 GHz, determined by the propagation velocity $c_{\mathrm{eff}} = c/\sqrt{\epsilon_{\mathrm{eff}}}$ ($\epsilon_{\mathrm{eff}} = 5.5$) of light in the transmission line. This finite size effect leads to convergence of Eqs. (5) at about 60 resonator modes [thin black line in Fig. 2(c)]. Second, the energy needed to overcome the pairing interaction of Cooper pairs sets an upper frequency of about 700 GHz for niobium. Also, radiation- or dielectric-loss mechanisms and the photon loss rate through the coupling capacitors increase at higher frequencies [39]. Our current experiments are, however, not designed to work at frequencies higher than approximately 15 GHz. The exploration of a much wider frequency range will require an elaborate circuit architecture and will be challenging with current technology.

IV. MULTIMODE COUPLING

To analyze the coupling to higher-order modes, we measure the qubit-qubit coupling strength J as a function of qubit transition frequency in a second sample B over a broader frequency range. In this sample the frequency of the fundamental resonator mode is lower, $\omega_0/(2\pi) = 3.34$ GHz, and the maximal Josephson energy E_J is higher by about one order of magnitude (see Table I, sample B). As a result, the qubit transition frequency can be swept over several resonator modes.

The measured interqubit coupling strength shows an enhanced value around each harmonic mode, as well as an overall increase with frequency (Fig. 4) in agreement with the discussion in Sec. III. A calculation based on the dispersive Jaynes-Cummings Hamiltonian can explain the data qualitatively. However, including an even ($N = 6$, solid red line) or odd ($N = 7$, dotted blue line) number of resonator modes yields again significant differences in the calculated value of J, with neither of the curves resulting in good quantitative agreement.

The resonator modes discussed so far cannot fully explain the measured frequency dependence of the interqubit coupling. Large deviations located around $\sim$8.5 GHz and $\sim$12 GHz (Fig. 4) hint at a coupling mechanism mediated by a different set of modes at these frequencies. The asymmetrically modified coupling strength between every two resonances suggests harmonic antiresonances that mediate qubit-qubit coupling channels of similar magnitude as the coplanar waveguide resonance. Due to interference, these lead to an enhancement or suppression of the qubit-qubit coupling at intermediate frequencies.

To account for these spurious resonances, additional field modes are included in the model. Treating these modes equivalently to the coplanar waveguide modes in the derivation of the dispersive multimode Jaynes-Cummings Hamiltonian (1) results in an extra contribution $\tilde{J}$ to the qubit-qubit coupling,

$$J_{\mathrm{tot}} = J + \tilde{J} = J + \frac{1}{2} \sum_{l}^{M} \tilde{g}_l^{(1)} \tilde{g}_l^{(2)} \left(\frac{1}{\tilde{\Delta}_l^{(1)}} + \frac{1}{\tilde{\Delta}_l^{(2)}} \right).$$

J_{tot} is then fit to the data in Fig. 4 assuming that the coupling strengths of both qubits are equal in magnitude, $|\tilde{g}_l^{(1)}| = |\tilde{g}_l^{(2)}|$. The qualitative agreement to the measured values of J is considerably improved by including four extra modes ($l = 1,2,3,4$); see dashed green line in Fig. 4. From the fit we obtain the resonance frequencies $\tilde{\omega}_{1,2,3,4}/(2\pi) \approx \{5.2, 8.4, 11.9, 14.8\}$ GHz. Note that these additional modes are not observed in transmission measurements [33] of the resonator and their frequencies can therefore not be determined independently. Further insight in the nature of these modes is gained by comparing the coupling strengths to the spurious modes $\tilde{g}_l^{(i)}$ with the coupling strength to the coplanar waveguide modes $g_l^{(i)}$. The ratios $\tilde{g}_l^{(i)}/g_l^{(i)}$ for $l = 1,2,3,4$ are determined to be $\{1(1), 0.5(2), 0.8(2), 0.7(1)\}$. They are of similar size, hinting at a highly localized field of the spurious mode with small effective mode volume. Moreover, an alternating relative sign between the couplings of the qubits to the spurious modes, $|\tilde{g}_l^{(1)}| = (-1)^{l+1} |\tilde{g}_l^{(2)}|$, with the mode number $l = 0,1,\ldots$ has to be imposed to obtain agreement between fit and data. As a consequence, the field amplitude of the spurious modes has—like the the coplanar waveguide mode outlined in Fig. 3—either equal or opposite direction

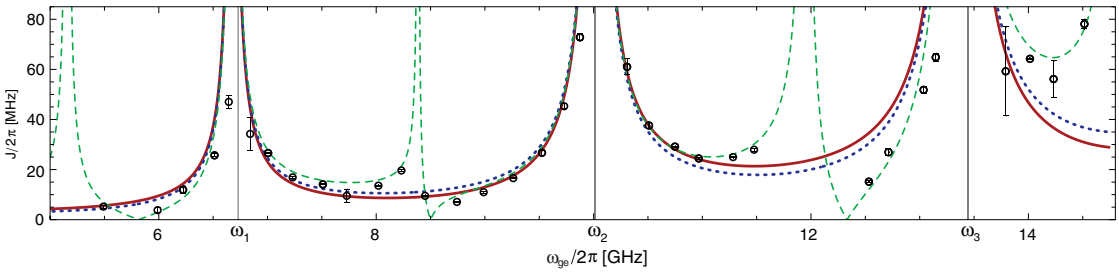

FIG. 4. (Color online) Qubit-qubit coupling strength J versus qubit frequency in sample B. The vertical lines indicate the frequencies of the coplanar waveguide modes ω_j. Experimental data (dots) confirm the expected increase of J with increasing frequency. The solid red (dotted blue) line is the calculated J including $N = 6$ ($N = 7$) resonator modes. The dashed green line is a fit to a model with additional resonances.

at the position of the qubits. This analysis provides strong evidence that the spurious modes can be identified physically as the slotline modes of the transmission line, a differential excitation of the left and right ground plane [40].

The measured values of the coupling strength J demonstrate the sensitivity of the qubit-qubit coupling to the full mode structure of the circuit. While a single-mode model is sufficient to describe the coupling around a single resonance, quantitative predictions require complete knowledge of designed and spurious resonances. Appropriate circuit design and use of wire bonds or air bridges connecting ground planes on the chip can suppress spurious modes, but have not been implemented in this sample. In contrast, additional resonances can also be incorporated on purpose into the circuit design [41,42] to modify the qubit-qubit coupling at certain frequencies.

V. DARK STATES

A characteristic feature of the avoided level crossing is a dark resonance, at which the transition from the ground state to the upper energy branch is forbidden and, as a result, no signal is observed in spectroscopy measurements; see Fig. 2(b). In fact, the symmetry of the states at the avoided crossing leads to a selection rule with respect to the spectroscopic drive applied to resonator described by [18,20]

$$H_d = \frac{\epsilon}{\Delta_d}(g^{(1)}\sigma_+^{(1)} + g^{(2)}\sigma_+^{(2)}) + \text{H.c.}, \tag{6}$$

where ϵ denotes the drive strength. This expression is written in the frame rotating at the drive frequency ω_d, and, for simplicity, only the dominant resonator mode with smallest detuning $|\Delta_d| \equiv \min_j(|\omega_j - \omega_d|)$ is taken into account.

To fully understand the relation between drive and state symmetry, we decompose the eigenvalues of the dispersive Hamiltonian (1) into triplet states and a singlet state. These are the eigenstates of the permutation operator Eq. (B1) to the eigenvalue ± 1. Explicitly, the triplet states $|gg\rangle$ (ground state), $|ee\rangle$ (doubly excited state), and the symmetric state $(|ge\rangle + |eg\rangle)/\sqrt{2}$ span the symmetric subspace, whereas the singlet state $(|ge\rangle - |eg\rangle)/\sqrt{2}$ is antisymmetric under permutation of the qubits. This is equivalent to a decomposition of the system into a spin-1 and spin-0 particle. The sign of the coupling constants $g^{(i)}$ determines the drive symmetry. Equal (opposite) sign of the electric field at the position of the two qubits leads to the positive (negative) sign of the second term in Eq. (6) and, consequently, to a(n) (anti)symmetric excitation. For equal sign of the couplings, the drive term and the permutation operator commute (symmetric drive). Then, only transitions between states of the same symmetry are allowed (see Appendix B) and the antisymmetric state stays dark at zero detuning. Vice versa, for opposite sign of the couplings the now antisymmetric drive can connect symmetric to antisymmetric states.

In our experiments the symmetry of the drive is determined by the frequency of the microwave signal and the distance d between the qubits. The relative sign of the field at the qubit positions x_i is determined by the phase difference $\Delta\phi = \phi(x_1) - \phi(x_2) = \omega_d d/c_{\text{eff}}$ between the qubits. Here, we have used the dispersion relation $k_d = \omega_d/c_{\text{eff}}$ with the propagation velocity c_{eff} of light in the transmission line. As the qubits are located at the end of the transmission line resonator, d is approximately the length of the resonator l_{res} and sign changes occur at frequencies $\omega_d = s\pi c_{\text{eff}}/(2l_{\text{res}})$ with $s = 1,3,5,\ldots$, in between two resonances as indicated by the dotted lines in Fig. 3(a).

Whether the eigenstate with lower or higher energy is dark, depends—in the simplest model with only a single dominant resonator mode—on the qubit-resonator detuning. The higher ($|\psi_+\rangle$) and lower ($|\psi_-\rangle$) energy eigenstate of the Hamiltonian (1) at the avoided crossing can, according to Eq. (3), be written as $\psi_\pm = (|ge\rangle \pm \text{sgn}(J)|eg\rangle)/\sqrt{2}$. Note that, in this notation, the subscript denotes higher (+) or lower (−) energy and not the symmetry of the state. In Fig. 5 the energy levels of the coupled resonator-qubits system are plotted as a function of the qubit transition frequencies, which are kept equal, along with their respective symmetries. For a coupling to the first-harmonic mode we find $J = g_1^{(1)}g_1^{(2)}/\Delta_1 < 0$ below the mode ($\Delta_1 < 0$, $g_1^{(1)}g_1^{(2)} > 0$) and $J > 0$ above the mode ($\Delta_1 > 0$, $g_1^{(1)}g_1^{(2)} > 0$). Consequently, below the first harmonic mode the higher-energy state ψ_+ is the antisymmetric singlet state. This state cannot be excited from the ground state with a symmetric drive and stays dark [Fig. 5(b), region A]. At the avoided crossing with a resonator mode the lower- and higher-energy qubit state swap their symmetry due to the sign change of the detuning. Since the drive does not change its symmetry, the dark and bright state energies are also interchanged and the dark state appears at the lower branch [Fig. 5(b), region B]. The dark state is always closer in frequency to the resonator transition.

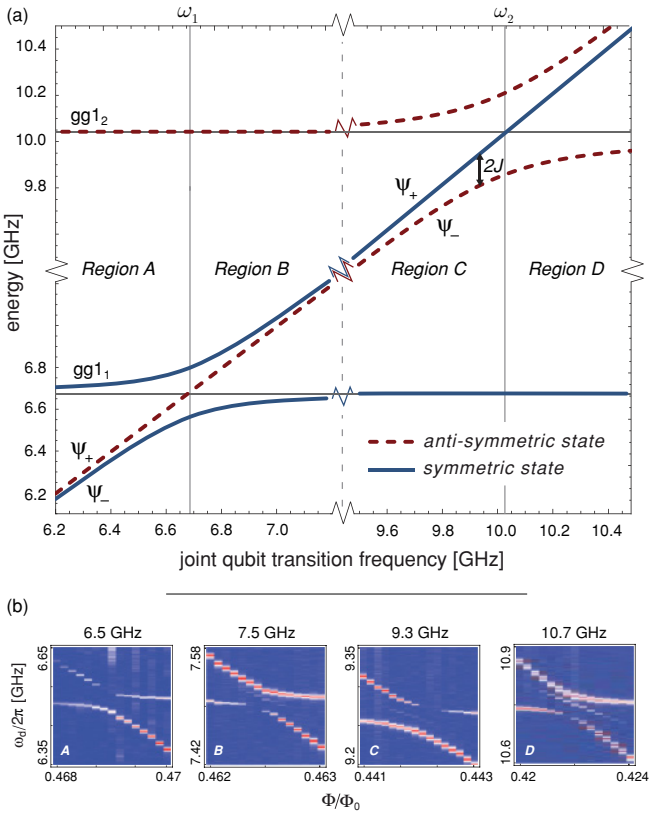

FIG. 5. (Color online) (a) Energy levels of the qubit-resonator system when the qubits are degenerate and their transition frequencies are simultaneously swept across the resonator modes. The parameters are those of sample B (Table I). (b) Spectroscopic measurements of the anticrossing in the regions labeled A, B, C, and D in (a).

If the second-harmonic mode dominates the coupling, the situation is reversed since the coupling constants have different signs. Below this mode, the ψ_+ (higher energy) state is symmetric, and ψ_- (lower energy) is antisymmetric. Still, the dark state appears at the upper branch of the avoided crossing [Fig. 5(b), region C] and switches to the lower branch above the resonator [Fig. 5(b), region D]. The reason is that the drive symmetry changes as well between two resonator modes as explained above, implying that the drive field changes from a symmetric (around the first-harmonic mode) to an antisymmetric drive (around the second-harmonic mode). The drive can then induce transitions between the ground and an antisymmetric state ψ_-, but not to the symmetric state ψ_+ of the upper branch. The various conditions leading to the identification of the dark state branch are summarized in Table II. In particular, if the drive (line 4) has a symmetry different from the higher energy state ψ_+ (line 3), ψ_+ remains dark.

VI. TWO-PHOTON TRANSITION

The spectroscopic line between upper and lower branch of the avoided level crossing in Fig. 2(b) is a two-photon transition from the ground state $|gg\rangle$ to the doubly excited state $|ee\rangle$. This transition has also been observed in a phase qubit coupled coherently to a two-level fluctuator in the tunnel barrier of the Josephson junction comprising the qubit [43] and in molecular spectroscopy of two nearby molecules [44]. It becomes visible only at the center of the avoided level crossing; again a manifestation of the symmetry properties of the system. The rate of the corresponding two-photon transition [45]

$$\Gamma = \frac{2\pi}{\hbar^4}\left|\sum_m \frac{\langle ee|H_d|m\rangle\langle m|H_d|gg\rangle}{\omega_m - \omega_d}\right|^2 \delta(\omega_{ee} - 2\omega_d)$$

is given by a sum over the intermediate states m. Off the avoided crossing the qubits are effectively decoupled. In this case the intermediate states are $m = ge, eg$. The transition is then prohibited due to destructive interference between the two possible paths, $gg \leftrightarrow eg \leftrightarrow ee$ or $gg \leftrightarrow ge \leftrightarrow ee$, connecting the ground to the doubly excited state. Due to the opposite sign of the detunings $\omega_{ge/eg} - \omega_d$, the two terms in the sum cancel and the transition rate $\Gamma = 0$. With the qubits at resonance, the intermediate states are $m = \psi^+, \psi^-$ and one term in the sum vanishes due to the forbidden transition to the dark state. With only one possible path connecting the gg to the ee state, no interference takes place and the transition is allowed. The enhanced transition rate can potentially be employed for directly creating the maximally entangled state $|\phi\rangle = (|gg\rangle + |ee\rangle)/\sqrt{2}$.

TABLE II. Symmetry considerations leading to the dark state at the lower- or upper-energy branch of the avoided level crossing. $\oplus$ ($\ominus$) denotes a positive (negative) value or symmetry. The sign of the coupling strength $J = g_j^{(1)} g_j^{(2)}/\Delta_j$ in row 3 defines the symmetry of the higher-energy state ψ_+. The product with the drive symmetry (row 4) then determines the dark state (row 5).

Region	A	B	C	D
$g_j^{(1)} g_j^{(2)}$	$\oplus$	$\oplus$	$\ominus$	$\ominus$
$\Delta_j^{(1,2)}$	$\ominus$	$\oplus$	$\ominus$	$\oplus$
$J \mathrel{\hat{=}} \psi_+$ symm.	$\ominus$	$\oplus$	$\oplus$	$\ominus$
drive symm.	$\oplus$	$\oplus$	$\ominus$	$\ominus$
dark state	ψ_+	ψ_-	ψ_+	ψ_-

VII. CONCLUSION

We have analyzed the coupling between two distant qubits mediated by the harmonic modes of a resonator. We have observed an overall increase of the qubit-qubit coupling with frequency as expected from a model including higher-harmonic modes of the coplanar waveguide resonator. Good qualitative agreement over a wide frequency range between the dispersive model and experimental data is obtained when taking spurious resonances of the coplanar waveguide in addition to the coplanar waveguide modes into account. Hence, measurements of the transverse interqubit coupling can be employed to detect and investigate spurious global coupling channels between distant qubits, complementary to measurements of single qubit spectra used to detect spurious local resonances [46,47]. How many higher-harmonic modes to include in the theory (i.e., where to set a high-frequency cutoff) can, however, not be decided on the basis of current measurements.

In addition, we have observed dark states and enhanced two-photon absorption at the avoided level crossing in spectroscopic measurements. These characteristic features are based on the relation between the symmetry of the drive and the singlet and triplet states formed by the coupled qubits, which also explains the dark state at either the lower- or higher-energy branch. These symmetries also affect decay processes of singlet and triplet states and, together with the nontrivial environment formed by the microwave resonator, dissipative dynamics of separable and entangled states can be studied. The J coupling can also be useful for building two-qubit gates when fast flux pulses are applied to tune the qubits into resonance. In the context of quantum information processing, the resulting SWAP gate forms a universal two-qubit gate with short operation times. Moreover, the J-coupling mechanism described in this article mediates the interaction not only between two, but also an arbitrary number of distant qubits; an interesting playground for studies of collective phenomena with superconducting circuits, where the interaction is not restricted to nearest neighbors.

ACKNOWLEDGMENTS

The authors acknowledge useful discussions with A. Blais and G. Bourassa. Also, the group of M. Siegel is acknowledged for the preparation of niobium films. This work was supported by the Swiss National Science Foundation (SNF), the Austrian Science Foundation (FWF), and ETH Zurich.

APPENDIX A: FREQUENCY DEPENDENCE OF THE QUBIT-RESONATOR COUPLING

The coupling g to the resonator is proportional to the rms voltage fluctuations of the vacuum field $V^0_{\rm rms}$ at the position of the ith qubit and to the off-diagonal matrix element [10,32] of the charge operator $\hat{n}$,

$$g = 2e\beta V^0_{\rm rms}\langle g|\hat{n}|e\rangle. \tag{A1}$$

The prefactor β is determined by the geometry of the circuit used in the experiments. In the large E_J/E_C limit realized in our devices, the matrix element is proportional to the square-root of the qubit transition frequency; $\langle g|\hat{n}|e\rangle \propto \sqrt{\omega_{ge}}$. The vacuum voltage fluctuations $V^0_{\rm rms}$ are proportional to the square root of the mode frequency; $\sqrt{\omega_j} = \sqrt{(j+1)\omega_0}$ [1,10].

For a single qubit on resonance with the jth resonator mode $\omega_{ge} = (j+1)\omega_0$ and the scaling of the qubit-resonator coupling is approximately linear in the mode number, $g \propto (j+1)\omega_0$. To verify the linearity of the coupling strength we have measured the vacuum Rabi splitting of a single qubit up to the third-harmonic resonator mode [Fig. 6(a)] using qubit 2 of sample B (for the parameters, see Table I). The simple estimate shows good agreement with the measured coupling strengths $g^{(2)}_{0,1,2,3}/(2\pi) = \{42, 84, 125, 162\}$MHz [dashed green line in Fig. 6(a)]. The parameter $\beta = 0.20$, obtained from a linear fit to the analytic model in the large E_J/E_C limit [32], agrees with the designed value within 10%. A numerical simulation of the transmon including four energy levels can explain also the slight deviations from the linear dependence at high frequencies [solid red line, Fig. 6(a)].

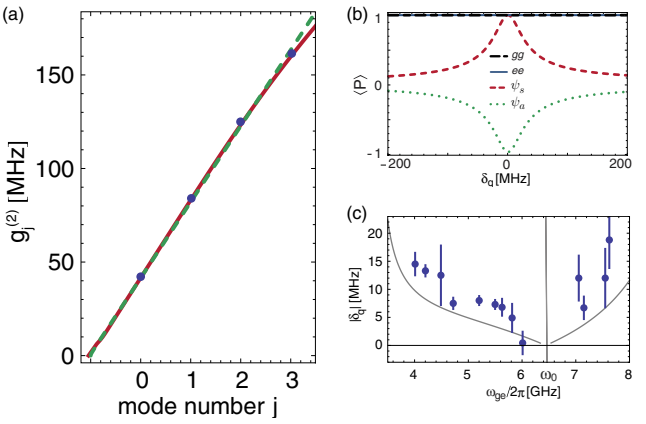

FIG. 6. (Color online) (a) Coupling strength $g^{(2)}_j$ of qubit 2 to the jth harmonic mode in sample B. (b) Expectation value of the permutation operator P for the eigenstates of the dispersive Jaynes-Cummings Hamiltonian as a function of qubit-qubit detuning δ_q. (c) Observed shift $|\delta_q|$ of the dark state relative to qubit-qubit resonance. The calculated shift due to an asymmetric field distribution of the driven transmission line at the qubit positions is indicated by the solid line.

In the case of two resonant qubits with identical coupling strength to the jth harmonic mode, the strength of the J coupling is, according to Eq. (2), linear in the qubit transition frequency ω_{ge} and the mode frequency $(j+1)\omega_0$,

$$J \propto g^{(1)}_j g^{(2)}_j \approx g^2_j \propto \omega_{ge}\omega_j = (j+1)\omega_{ge}\omega_0. \tag{A2}$$

When the detuning of the qubits to the resonator mode is varied, the frequency $(j+1)\omega_0$ of the jth resonator mode is constant and J scales proportional to the transition frequency ω_{ge}.

APPENDIX B: DARK STATE SYMMETRY

The spectroscopic drive $H_d \propto (\sigma^{(1)}_+ - \sigma^{(2)}_+) + \text{H.c.}$ [18] anticommutes with the permutation operator

$$P \equiv (\sigma^{(1)}_+\sigma^{(2)}_- + \sigma^{(2)}_+\sigma^{(1)}_-) + \left(1 + \sigma^{(1)}_z\sigma^{(2)}_z\right)/2, \tag{B1}$$

$$[H_d, P]_+ \equiv H_d P + P H_d = 0. \tag{B2}$$

This relation can be fulfilled only if the drive transforms a symmetric (ψ_s) to an antisymmetric (ψ_a) state, or vice versa, such that

$$\begin{aligned}[H_d, P]_+\,\psi_s &= H_d P\psi_s + P H_d\psi_s \\ &= H_d\psi_s + P\psi_a \\ &= \psi_a - \psi_a = 0.\end{aligned} \tag{B3}$$

The symmetry of the coupled qubit states [see Fig. 2(a)] can be characterized by the corresponding expectation value of the permutation operator $\langle P\rangle$. $\langle P\rangle$ is unity for the $|gg\rangle$ and the $|ee\rangle$ state (i.e., the $|gg\rangle$ and $|ee\rangle$ states are symmetric for all detunings). For the symmetric and antisymmetric states ψ_s and ψ_a formed at zero qubit-qubit detuning, $\langle P\rangle$ is 1 or -1 indicating that these states are eigenstates of P with well-defined symmetry. For nonzero detuning between the qubits, $\delta_q \neq 0$, the eigenstates of the Hamiltonian (1) do not have well-defined symmetry and $\langle P\rangle$ asymptotically

approaches zero for large detunings [Fig. 6(b)]. Hence, no strict selection rules are imposed off the level crossing and the transition between ground state and single excited states is allowed. Similar considerations hold for a symmetric drive $\propto \sigma_+^{(1)} + \sigma_-^{(2)}$.

APPENDIX C: RELATIVE POSITION OF THE DARK STATE

It is observed (see Fig. 2) that the frequency of the dark state is shifted away from the center of the avoided crossing. In fact, for given drive term H_d (6) the dark state $|\psi_{\rm dark}\rangle$ is defined by the condition

$$\langle gg|H_d|\psi_{\rm dark}\rangle = 0. \tag{C1}$$

Both a change in the symmetry of the state and in the symmetry of the drive can lead to a shift in frequency of the observed dark state. In our devices, where the coupling strengths $|g^{(1)}| \approx |g^{(2)}|$ are approximately equal, the observed shift of the dark-state frequency originates from an asymmetry of the drive.

Assuming the contrary (i.e., a perfectly antisymmetric drive), it immediately follows from Eq. (C1) that the dark state is the symmetric triplet state, $|\psi_{\rm dark}\rangle = |\psi_s\rangle$. According to Eq. (3), this state is realized at qubit-resonance with $\delta_q = 0$, thus no shift of the dark-state position is expected. To account for the slight asymmetry $\alpha \equiv g^{(2)}/g^{(1)}$ in the coupling strengths the dark state condition in Eq. (C1) can be written in terms of the mixing angle θ_m (Eq. (3)) as

$$\tan\theta_m(\delta_q) = 1/\alpha, \tag{C2}$$

using Eq. (6) at equal qubit detuning. The asymmetry in the coupling of $\alpha \approx 0.99$ for sample A leads—for the parameters from Fig. 2(b)—to a shift of only 200 kHz and does not account for the observed shift of 8 MHz. Similar considerations hold for sample B with an asymmetry $\alpha_B \approx 1.02$. We have also verified by a numerical diagonalization of the full Jaynes-Cummings Hamiltonian that the modification of the state symmetry due to higher-harmonic modes cannot explain the observed dark-state shift. Therefore, the shift must be caused by an asymmetry in the drive.

In fact, the field amplitude inside an asymmetrically driven (ideal) transmission line resonator of length $l_{\rm res}$ is given by $f(x) = \cos[\omega(x - l_{\rm res})/c_{\rm eff}]$ such that a voltage antinode is retained at its undriven port at $x = l_{\rm res}$. The position-dependent field modifies the coupling strength of the individual qubits to the drive in Eq. (6) to $f(x_i)g^{(i)}$ resulting in an effective coupling asymmetry $\alpha = f(d)/f(0)$ and a shift of the observed dark state δ_q according to Eq. (C2). With the qubits located at either end of the resonator, $x_1 = 0$ and $x_2 = l_{\rm res}$ this simple estimate leads to a qualitative agreement with the observed shifts of the dark state; see Fig. 6(c). For better agreement, a refined model has to take the field amplitude at the qubits' position given by the actual geometry of the circuit into account.

[1] S. Haroche and J.-M. Raimond, *Exploring the Quantum: Atoms, Cavities, and Photons* (OUP Oxford, 2006).

[2] D. Meschede, H. Walther, and G. Müller, Phys. Rev. Lett. **54**, 551 (1985).

[3] J. M. Raimond, M. Brune, and S. Haroche, Rev. Mod. Phys. **73**, 565 (2001).

[4] R. Miller, T. E. Northup, K. M. Birnbaum, A. Boca, A. D. Boozer, and H. J. Kimble, J. Phys. B **38**, S551 (2005).

[5] H. Walther, B. T. H. Varcoe, B.-G. Englert, and T. Becker, Rep. Prog. Phys. **69**, 1325 (2006).

[6] J. P. Reithmaier, G. Sek, A. Loffler, C. Hofmann, S. Kuhn, S. Reitzenstein, L. V. Keldysh, V. D. Kulakovskii, T. L. Reinecke, and A. Forchel, Nature (London) **432**, 197 (2004).

[7] T. Yoshie, A. Scherer, J. Hendrickson, G. Khitrova, H. M. Gibbs, G. Rupper, C. Ell, O. B. Shchekin, and D. G. Deppe, Nature (London) **432**, 200 (2004).

[8] A. Wallraff, D. I. Schuster, A. Blais, L. Frunzio, R. S. Huang, J. Majer, S. Kumar, S. M. Girvin, and R. J. Schoelkopf, Nature (London) **431**, 162 (2004).

[9] E. Jaynes and F. Cummings, Proc. IEEE **51**, 89 (1963).

[10] A. Blais, R.-S. Huang, A. Wallraff, S. M. Girvin, and R. J. Schoelkopf, Phys. Rev. A **69**, 062320 (2004).

[11] A. Houck, D. Schuster, J. Gambetta, J. Schreier, B. Johnson, J. Chow, L. Frunzio, J. Majer, M. Devoret, S. Girvin, and R. J. Schoelkopf, Nature (London) **449**, 328 (2007).

[12] J. M. Fink, M. Göppl, M. Baur, R. Bianchetti, P. J. Leek, A. Blais, and A. Wallraff, Nature (London) **454**, 315 (2008).

[13] M. Hofheinz, H.Wang, M. Ansmann, R. C. Bialczak, E. Lucero, M. Neeley, A. D. O'Connell, D. Sank, J.Wenner, J. M. Martinis, and A. N. Cleland, Nature (London) **459**, 546 (2009).

[14] M. A. Sillanpää, J. I. Park, and R. W. Simmonds, Nature (London) **449**, 438 (2007).

[15] J. M. Fink, R. Bianchetti, M. Baur, M. Goppl, L. Steffen, S. Filipp, P. J. Leek, A. Blais, and A. Wallraff, Phys. Rev. Lett. **103**, 083601 (2009).

[16] A. Fragner, M. Göppl, J. M. Fink, M. Baur, R. Bianchetti, P. J. Leek, A. Blais, and A. Wallraff, Science **322**, 1357 (2008).

[17] D. I. Schuster, A. Wallraff, A. Blais, L. Frunzio, R.-S. Huang, J. Majer, S. M. Girvin, and R. J. Schoelkopf, Phys. Rev. Lett. **94**, 123602 (2005).

[18] A. Blais, J. Gambetta, A. Wallraff, D. I. Schuster, S. M. Girvin, M. H. Devoret, and R. J. Schoelkopf, Phys. Rev. A **75**, 032329 (2007).

[19] O. Gywat, F. Meier, D. Loss, and D. D. Awschalom, Phys. Rev. B **73**, 125336 (2006).

[20] J. Majer, J. M. Chow, J. M. Gambetta, J. Koch, B. R. Johnson, J. A. Schreier, L. Frunzio, D. I. Schuster, A. A. Houck, A. Wallraff, A. Blais, M. H. Devoret, S. M. Girvin, and R. J. Schoelkopf, Nature (London) **449**, 443 (2007).

[21] A. Abragam, *Principles of Nuclear Magnetism* (Oxford University Press, 1961).

[22] L. M. K. Vandersypen and I. L. Chuang, Rev. Mod. Phys. **76**, 1037 (2004).

[23] T. Yamamoto, Y. A. Pashkin, O. Astafiev, Y. Nakamura, and J. S. Tsai, Nature (London) **425**, 941 (2003).

[24] R. McDermott, R. W. Simmonds, M. Steffen, K. B. Cooper, K. Cicak, K. D. Osborn, S. Oh, D. P. Pappas, and J. M. Martinis, Science **307**, 1299 (2005).
[25] M. Steffen, M. Ansmann, R. McDermott, N. Katz, R. C. Bialczak, E. Lucero, M. Neeley, E. M. Weig, A. N. Cleland, and J. M. Martinis, Phys. Rev. Lett. **97**, 050502 (2006).
[26] T. Hime, P. A. Reichardt, B. L. T. Plourde, T. L. Robertson, C. E. Wu, A. V. Ustinov, and J. Clarke, Science **314**, 1427 (2006).
[27] A. O. Niskanen, K. Harrabi, F. Yoshihara, Y. Nakamura, S. Lloyd, and J. S. Tsai, Science **316**, 723 (2007).
[28] J. H. Plantenberg, P. C. de Groot, C. J. P. M. Harmans, and J. E. Mooij, Nature (London) **447**, 836 (2007).
[29] M. Neeley, R. C. Bialczak, M. Lenander, E. Lucero, M. Mariantoni, A. D. O'Connell, D. Sank, H. Wang, M. Weides, J. Wenner, Y. Yin, T. Yamamoto, A. N. Cleland, and J. M. Martinis, Nature (London) **467**, 570 (2010).
[30] L. DiCarlo, J. M. Chow, J. M. Gambetta, L. S. Bishop, B. R. Johnson, D. I. Schuster, J. Majer, A. Blais, L. Frunzio, S. M. Girvin, and R. J. Schoelkopf, Nature (London) **460**, 240 (2009).
[31] L. DiCarlo, M. D. Reed, L. Sun, B. R. Johnson, J. M. Chow, J. M. Gambetta, L. Frunzio, S. M. Girvin, M. H. Devoret, and R. J. Schoelkopf, Nature (London) **476**, 574 (2010).
[32] J. Koch, T. M. Yu, J. Gambetta, A. A. Houck, D. I. Schuster, J. Majer, A. Blais, M. H. Devoret, S. M. Girvin, and R. J. Schoelkopf, Phys. Rev. A **76**, 042319 (2007).
[33] M. Göppl, A. Fragner, M. Baur, R. Bianchetti, S. Filipp, J. M. Fink, P. J. Leek, G. Puebla, L. Steffen, and A. Wallraff, J. Appl. Phys. **104**, 113904 (2008).
[34] R. Bianchetti, S. Filipp, M. Baur, J. M. Fink, M. Göppl, P. J. Leek, L. Steffen, A. Blais, and A. Wallraff, Phys. Rev. A **80**, 043840 (2009).
[35] S. Filipp, P. Maurer, P. J. Leek, M. Baur, R. Bianchetti, J. M. Fink, M. Göppl, L. Steffen, J. M. Gambetta, A. Blais, and A. Wallraff, Phys. Rev. Lett. **102**, 200402 (2009).
[36] S.-B. Zheng and G.-C. Guo, Phys. Rev. Lett. **85**, 2392 (2000).
[37] S. Osnaghi, P. Bertet, A. Auffeves, P. Maioli, M. Brune, J. M. Raimond, and S. Haroche, Phys. Rev. Lett. **87**, 037902 (2001).
[38] F. Brennecke, T. Donner, S. Ritter, T. Bourdel, M. Köhl, and T. Esslinger, Nature (London) **450**, 268 (2007).
[39] A. A. Houck, J. A. Schreier, B. R. Johnson, J. M. Chow, J. Koch, J. M. Gambetta, D. I. Schuster, L. Frunzio, M. H. Devoret, S. M. Girvin, and R. J. Schoelkopf, Phys. Rev. Lett. **101**, 080502 (2008).
[40] I. Wolff, *Coplanar Microwave Integrated Circuits* (Wiley InterScience, 2006).
[41] P. J. Leek, M. Baur, J. M. Fink, R. Bianchetti, L. Steffen, S. Filipp, and A. Wallraff, Phys. Rev. Lett. **104**, 100504 (2010).
[42] M. D. Reed, B. R. Johnson, A. A. Houck, L. DiCarlo, J. M. Chow, D. I. Schuster, L. Frunzio, and R. J. Schoelkopf, Appl. Phys. Lett. **96**, 203110 (2010).
[43] P. Bushev, C. Müller, J. Lisenfeld, J. H. Cole, A. Lukashenko, A. Shnirman, and A. V. Ustinov, Phys. Rev. B **82**, 134530 (2010).
[44] C. Hettich, C. Schmitt, J. Zitzmann, S. Kuhn, I. Gerhardt, and V. Sandoghdar, Science **298**, 385 (2002).
[45] R. Loudon, *The Quantum Theory of Light* (Oxford University Press, 2000).
[46] R. W. Simmonds, K. M. Lang, D. A. Hite, S. Nam, D. P. Pappas, and J. M. Martinis, Phys. Rev. Lett. **93**, 077003 (2004).
[47] J. M. Martinis, K. B. Cooper, R. McDermott, M. Steffen, M. Ansmann, K. D. Osborn, K. Cicak, S. Oh, D. P. Pappas, R. W. Simmonds, and C. C. Yu, Phys. Rev. Lett. **95**, 210503 (2005).